electronics

MDPI

Article

Effect of Coupling Impedance on Stability Assessment of Grid-Forming Converters Under Various Grid Conditions

Haiguo Tang, Jinhao Wang, Chao Wu * and Yong Wang

Department of Electrical Engineering, Shanghai Jiaotong University, Shanghai 200240, China; tanghg1@sjtu.edu.cn (H.T.); daan6666@sjtu.edu.cn (J.W.); wangyong75@sjtu.edu.cn (Y.W.)
* Correspondence: wuchao@sjtu.edu.cn

Abstract: The phenomenon of frequency coupling is widely observed in grid-forming (GFM) converters due to the presence of asymmetrical controls and nonlinear blocks. However, the factors influencing frequency coupling have not been thoroughly explored. This paper introduces a systematic small-signal impedance model of GFM converters that intuitively reflects the factors affecting frequency coupling and provides a detailed analysis of how coupling impedance affects stability. It is demonstrated that the influencing factors of coupling impedance are an active power loop and reactive power loop. Specifically, the active power loop influences coupling impedance characteristics near the fundamental frequency, while the reactive power loop impacts the entire frequency range. This paper first reveals that the reactive power loop has a more pronounced effect on frequency coupling than the active power loop. Additionally, the variation in the steady-state operating points also affects the degree of frequency coupling of the GFM converters, primarily affecting the coupling impedance characteristics beyond the fundamental frequency, and the low operating points tend to affect system stability adversely. Finally, simulation results validate the accuracy of the mathematical model and theoretical analysis.

Keywords: grid-forming (GFM) converter; oscillation; impedance model; frequency coupling

check for updates

Citation: Tang, H.; Wang, J.; Wu, C.; Wang, Y. Effect of Coupling Impedance on Stability Assessment of Grid-Forming Converters Under Various Grid Conditions. *Electronics* **2024**, *13*, 4382. https://doi.org/10.3390/electronics13224382

Academic Editor: Carlos Andrés García-Vázquez

Received: 11 September 2024
Revised: 17 October 2024
Accepted: 5 November 2024
Published: 8 November 2024

Copyright: © 2024 by the authors. Licensee MDPI, Basel, Switzerland. This article is an open access article distributed under the terms and conditions of the Creative Commons Attribution (CC BY) license (https://creativecommons.org/licenses/by/4.0/).

1. Introduction

With the proportion of renewable energy capacities such as photovoltaic and wind power gradually increasing in power systems, the importance of GFM converters is gradually becoming more and more prominent in power systems [1]. Unlike the traditional grid-following (GFL) converters based on phase-locked loops (PLLs), GFM converters present voltage-source characteristics that can actively support voltage and frequency. The GFM converters also improve the inertia and damping of the system, which can better support the power-electronics-based power system [2].

GFM converters generally utilize a cascaded control structure with different functionalities [3]. The outer loop is designed to achieve grid synchronization and to constrain active and reactive power. Unlike GFL converters, which use a PLL to track the phase of the PCC voltage, GFM converters typically generate their own voltage source phase through a power synchronization control. This can be accomplished using various methods, such as a droop control [4], virtual synchronous generator (VSG) control [5], matching control [6], and virtual oscillator control [7]. The inner loop consists of a voltage control loop and current control loop, aimed at suppressing voltage harmonics [8], limiting fault currents [9], and damping LC resonance [10]. It also includes different control strategies like an open-loop control [11], single voltage loop control [12], voltage–current dual-loop control [13], and virtual admittance control [14].

However, employing such cascaded controls can lead to interactions between the GFM converter and the grid, triggering a series of low-frequency oscillation issues [15]. The impedance-based approach has been widely utilized to investigate the low-frequency oscillation issues of the GFM grid-connected system. References [16,17] developed impedance

models for GFL and GFM converters, comparing and analyzing the impedance characteristics of these two distinct control schemes, but both overlooked the dynamics of the inner loop. In [18], the impedance modeling of all control loops in the GFM converter was performed, with the system being decomposed into positive-sequence and negative-sequence subsystems for stability analysis. Moreover, it is revealed that inner loops should not be ignored, since they have a significant influence on the output impedance of GFM converters. However, none of the above studies considered the impact of frequency coupling, which could lead to significant discrepancies with the actual impedance and result in incorrect stability assessments.

The full impedances of GFM converters considering frequency coupling were built in [13,19–21]. While previous studies have considered the impact of coupling impedance, they have not clearly identified the underlying factors that cause frequency coupling. Additionally, most of the research has concentrated on the frequency coupling issues introduced by the active power loop, with limited attention given to the frequency coupling effects caused by the reactive power loop. This paper reveals that the active power loop primarily influences the coupling characteristics of the GFM impedance model near the fundamental frequency, whereas the reactive power loop affects the coupling characteristics across the entire frequency range. Moreover, the frequency coupling characteristics are particularly sensitive to variations in the reactive power loop parameters. As the gain of the reactive power loop increases, the degree of frequency coupling intensifies, making it critical to consider frequency coupling in stability analysis to avoid potential misjudgments.

The rest of this paper is organized as follows. In Section 2, the systematic small-signal impedance model of the GFM converter considering frequency coupling is developed and validated through a frequency scan. Then it is further analyzed which factors are critical to causing frequency coupling. Section 3 explores the effects of the steady-state operating points, active power loop, and reactive power loop on the characteristics of the coupling impedance. The corresponding GNC stability analysis and simulation verification are developed in Section 4. Finally, the conclusions are drawn in Section 5.

2. Small-Signal Modeling and Impedance Characteristics of GFM Converter

The configuration of the GFM converter connected to the grid is shown in Figure 1, where V_{dc} is the DC-side voltage, $\boldsymbol{V}_c$ is the converter port voltage, $\boldsymbol{V}_C$ is the PCC voltage, and $\boldsymbol{V}_g$ is the grid voltage. Additionally, $\boldsymbol{I}_L$ is the GFM output current, and $\boldsymbol{I}_g$ is the grid-side current. The filter components include the filter inductor L_f, filter resistor R_f, and filter capacitor C_f. The grid impedance includes grid inductor L_g and grid resistor R_g. The control part consists of the outer loop for power synchronization and the inner loop for controlling the voltage and current. The outer loop adopts the structure shown in the figure to provide inertia and damping of the system, while the inner loop utilizes the cascaded voltage–current dual PI control structure. The active power loop generates the power angle θ to synchronize the converter with the grid, which is then utilized for coordinate transformations. Meanwhile, the reactive power loop produces an internal voltage E, serving as the reference signal for the voltage control in the inner loop. The voltage control loop measures the PCC voltage and, through a PI controller, generates the current reference signal. The current control loop, in turn, measures the converter output current and uses a PI controller to produce a modulation voltage signal, which adjusts the converter port voltage accordingly.

In this paper, the small-signal impedance model is introduced for stability analysis, since it has a clear physical implication. In the following sections, the symbol 'Δ' denotes a small-signal perturbation of a variable, and the subscript '$_0$' denotes a steady-state operating point. Moreover, the subscripts '$_d$' or '$_q$' denote the *d*-axis or *q*-axis component of the variables under the *d*-*q* frame system.

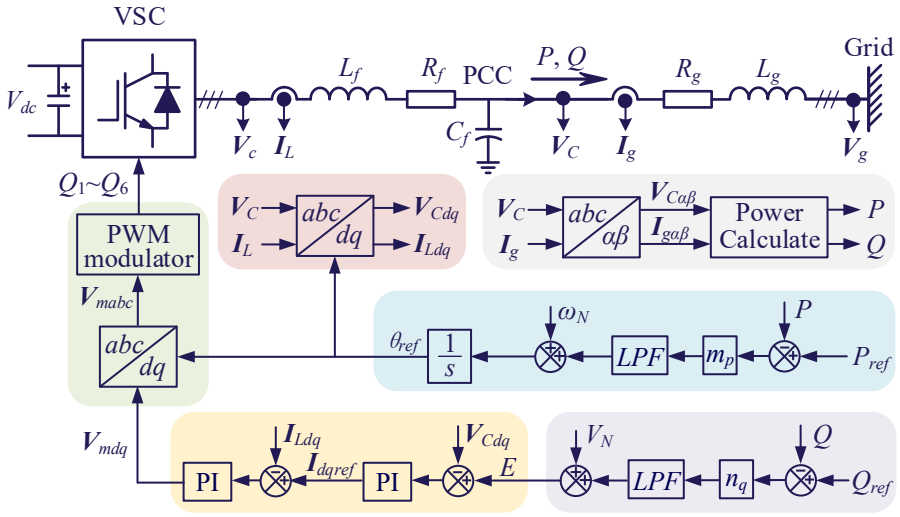


Figure 1. Block diagram of the GFM grid-connected system.

2.1. Small-Signal Impedance Modeling of GFM

Firstly, based on the physical circuit structure shown in Figure 1, the small-signal equations in the grid *d*-*q* frame can be derived.

$$\begin{bmatrix}\Delta v_{Cd}\\ \Delta v_{Cq}\end{bmatrix}-\begin{bmatrix}\Delta v_{gd}\\ \Delta v_{gq}\end{bmatrix}=\begin{bmatrix}sL_g+R_g & -\omega_1 L_g\\ \omega_1 L_g & sL_g+R_g\end{bmatrix}\cdot\begin{bmatrix}\Delta i_{gd}\\ \Delta i_{gq}\end{bmatrix} \tag{1}$$

$$\begin{bmatrix}\Delta i_{Ld}\\ \Delta i_{Lq}\end{bmatrix}-\begin{bmatrix}\Delta i_{gd}\\ \Delta i_{gq}\end{bmatrix}=\begin{bmatrix}sC_f & -\omega_1 C_f\\ \omega_1 C_f & sC_f\end{bmatrix}\cdot\begin{bmatrix}\Delta v_{Cd}\\ \Delta v_{Cq}\end{bmatrix} \tag{2}$$

$$\begin{bmatrix}\Delta v_{cd}\\ \Delta v_{cq}\end{bmatrix}-\begin{bmatrix}\Delta v_{Cd}\\ \Delta v_{Cq}\end{bmatrix}=\begin{bmatrix}sL_f+R_f & -\omega_1 L_f\\ \omega_1 L_f & sL_f+R_f\end{bmatrix}\cdot\begin{bmatrix}\Delta i_{Ld}\\ \Delta i_{Lq}\end{bmatrix} \tag{3}$$

where "*s*" represents the Laplace differential operator and $\omega_1 = 100\pi$ rad/s denotes the rated angular frequency. The second-order matrices in (1) to (3) can be expressed as follows: $\mathbf{B}_{Lg}$, $\mathbf{B}_{Cf}$ and $\mathbf{B}_{Lf}$.

Then, perform small-signal modeling for the power outer loop. The small-signal equation of the active power loop for the GFM converter is expressed as follows:

$$\Delta\omega = -\frac{m_p\omega_p}{s+\omega_p}\Delta P \tag{4}$$

where m_p denotes the droop gain of the active power loop and ω_p denotes the cut-off frequency of the low-pass filter (LPF) of the active power loop.

Based on (4), the small-signal equation for $\Delta\theta$ is obtained as follows:

$$\Delta\theta = \frac{\Delta\omega}{s} = \frac{-m_p\omega_p}{s(s+\omega_p)}\Delta P = -G_P\Delta P \tag{5}$$

where G_P represents the active power loop gain.

Additionally, the small-signal equation for the actual value of active power is the following:

$$\Delta P = \frac{3}{2}\begin{bmatrix}i_{gd0} & i_{gq0}\end{bmatrix}\begin{bmatrix}\Delta v_{Cd}\\ \Delta v_{Cq}\end{bmatrix}+\frac{3}{2}\begin{bmatrix}v_{Cd0} & v_{Cq0}\end{bmatrix}\begin{bmatrix}\Delta i_{gd}\\ \Delta i_{gq}\end{bmatrix} \tag{6}$$

where i_{gd0} and i_{gq0} denote the *d*-axis and *q*-axis steady-state value components of the grid current i_g in the *d*-*q* frame, and v_{Cd0} and v_{Cq0} denote the *d*-axis and *q*-axis steady-state value components of the PCC voltage v_C in the *d*-*q* frame.

Substituting (6) into (5) yields the detailed expression for $\Delta\theta$:

$$\Delta\theta = -G_P\left(\frac{3}{2}\begin{bmatrix} i_{gd0} & i_{gq0}\end{bmatrix}\begin{bmatrix}\Delta v_{Cd}\\ \Delta v_{Cq}\end{bmatrix} + \frac{3}{2}\begin{bmatrix} v_{Cd0} & v_{Cq0}\end{bmatrix}\begin{bmatrix}\Delta i_{gd}\\ \Delta i_{gq}\end{bmatrix}\right) \tag{7}$$

Similarly, the small-signal equation for the reactive power loop can be expressed as follows:

$$\Delta E = -\frac{n_q\omega_q}{s+\omega_q}\Delta Q \tag{8}$$

where n_q denotes the droop gain of the reactive power loop and ω_q denotes the cut-off frequency of the LPF of the reactive power loop.

The small-signal equation for the actual value of reactive power is as follows:

$$\Delta Q = \frac{3}{2}\begin{bmatrix} -i_{gq0} & i_{gd0}\end{bmatrix}\begin{bmatrix}\Delta v_{Cd}\\ \Delta v_{Cq}\end{bmatrix} + \frac{3}{2}\begin{bmatrix} v_{Cq0} & -v_{Cd0}\end{bmatrix}\begin{bmatrix}\Delta i_{gd}\\ \Delta i_{gq}\end{bmatrix} \tag{9}$$

Substituting (9) into (8) yields the detailed expression for ΔE:

$$\begin{aligned}\Delta E &= -\tfrac{3}{2}\tfrac{n_q\omega_q}{s+\omega_q}\left(\begin{bmatrix} -i_{gq0} & i_{gd0}\end{bmatrix}\begin{bmatrix}\Delta v_{Cd}\\ \Delta v_{Cq}\end{bmatrix} + \begin{bmatrix} v_{Cq0} & -v_{Cd0}\end{bmatrix}\begin{bmatrix}\Delta i_{gd}\\ \Delta i_{gq}\end{bmatrix}\right)\\ &= G_Q\left(\begin{bmatrix} -i_{gq0} & i_{gd0}\end{bmatrix}\begin{bmatrix}\Delta v_{Cd}\\ \Delta v_{Cq}\end{bmatrix} + \begin{bmatrix} v_{Cq0} & -v_{Cd0}\end{bmatrix}\begin{bmatrix}\Delta i_{gd}\\ \Delta i_{gq}\end{bmatrix}\right)\end{aligned} \tag{10}$$

where G_Q represents the reactive power loop gain.

Since v_{Cq}* = 0, the small-signal expression for the command signal Δv_{Cdq}* input to the voltage loop is as follows:

$$\begin{aligned}\Delta {v_{Cdq}}^* &= \begin{bmatrix}\Delta E\\ 0\end{bmatrix} = \begin{bmatrix} -G_Q i_{gq0} & G_Q i_{gd0}\\ 0 & 0\end{bmatrix}\begin{bmatrix}\Delta v_{Cd}\\ \Delta v_{Cq}\end{bmatrix} + \begin{bmatrix} G_Q v_{Cq0} & -G_Q v_{Cd0}\\ 0 & 0\end{bmatrix}\begin{bmatrix}\Delta i_{gd}\\ \Delta i_{gq}\end{bmatrix}\\ &= B_{ig}\Delta v_{Cdq} + B_{vC}\Delta i_{gdq}\end{aligned} \tag{11}$$

where $\mathbf{B_{ig}}$ and $\mathbf{B_{vC}}$ are the current matrix and voltage matrix introduced by the reactive power loop, respectively.

This is followed by small-signal modeling of the voltage–current inner loop. The small-signal equation for the voltage loop is expressed as follows:

$$\begin{bmatrix}\Delta {i_{Ld}}^*\\ \Delta {i_{Lq}}^*\end{bmatrix} = \begin{bmatrix} G_{pi_V} & 0\\ 0 & G_{pi_V}\end{bmatrix}\cdot\left(\begin{bmatrix}\Delta {v_{Cd}}^*\\ \Delta {v_{Cq}}^*\end{bmatrix} - \begin{bmatrix}\Delta {v_{Cd}}^{ctrl}\\ \Delta {v_{Cq}}^{ctrl}\end{bmatrix}\right) + \begin{bmatrix} 0 & -\omega_1 C_f\\ \omega_1 C_f & 0\end{bmatrix}\begin{bmatrix}\Delta {v_{Cd}}^{ctrl}\\ \Delta {v_{Cq}}^{ctrl}\end{bmatrix} \tag{12}$$

where $\Delta {i_{Ldq}}^*$ represents the output command of the voltage loop, which is used as the command input for the current loop. $G_{pi_V} = k_{p_V} + k_{i_V}/s$, k_{p_V} denotes the proportional gain of the voltage loop PI controller, and k_{i_V} denotes the integral gain of the voltage loop PI controller.

In addition, the small-signal equation for the current loop is expressed as follows:

$$\begin{bmatrix}\Delta {v_{Cd}}^{ctrl}\\ \Delta {v_{Cq}}^{ctrl}\end{bmatrix} = \begin{bmatrix} G_{pi_I} & 0\\ 0 & G_{pi_I}\end{bmatrix}\cdot\left(\begin{bmatrix}\Delta {i_{Ld}}^*\\ \Delta {i_{Lq}}^*\end{bmatrix} - \begin{bmatrix}\Delta {i_{Ld}}^{ctrl}\\ \Delta {i_{Lq}}^{ctrl}\end{bmatrix}\right) + \begin{bmatrix} 0 & -\omega_1 L_f\\ \omega_1 L_f & 0\end{bmatrix}\cdot\begin{bmatrix}\Delta {i_{Ld}}^{ctrl}\\ \Delta {i_{Lq}}^{ctrl}\end{bmatrix} \tag{13}$$

where $G_{pi_I} = k_{p_I} + k_{i_I}/s$, k_{p_I} denotes the proportional gain of the current loop PI controller, and k_{i_I} denotes the integral gain of the current loop PI controller. The second-order matrices in (12) to (13) can be expressed as $\mathbf{B_{PI\text{-}V}}$, $\mathbf{B_{decpl\text{-}V}}$, $\mathbf{B_{PI\text{-}I}}$, and $\mathbf{B_{decpl\text{-}I}}$.

Moreover, the small-signal equations for the coordinate transformation between the grid *d-q* frame and the control *d-q* frame are as follows:

$$\begin{bmatrix}\Delta {v_{Cd}}^{ctrl}\\ \Delta {v_{Cq}}^{ctrl}\end{bmatrix} = \begin{bmatrix}\Delta v_{Cd}\\ \Delta v_{Cq}\end{bmatrix} + \begin{bmatrix} v_{Cq0}\\ -v_{Cd0}\end{bmatrix}\cdot\Delta\theta \tag{14}$$

$$\begin{bmatrix} \Delta i_{Ld}{}^{ctrl} \\ \Delta i_{Lq}{}^{ctrl} \end{bmatrix} = \begin{bmatrix} \Delta i_{Ld} \\ \Delta i_{Lq} \end{bmatrix} + \begin{bmatrix} i_{Lq0} \\ -i_{Ld0} \end{bmatrix} \cdot \Delta\theta \tag{15}$$

$$\begin{bmatrix} \Delta v_{cd} \\ \Delta v_{cq} \end{bmatrix} = \begin{bmatrix} \Delta v_{Cd}{}^{ctrl} \\ \Delta v_{Cq}{}^{ctrl} \end{bmatrix} + \begin{bmatrix} -v_{cq0} \\ v_{cd0} \end{bmatrix} \cdot \Delta\theta \tag{16}$$

where i_{Ld0} and i_{Lq0} denote the d-axis and q-axis steady-state value components of the GFM output current i_L in the d-q frame, and v_{cd0} and v_{cq0} denote the d-axis and q-axis steady-state value components of the converter port voltage v_c in the d-q frame.

For clarity, the superscript '$ctrl$' denotes the variables in the control d-q frame.

Finally, substituting (7) into (14) to (16) yields the detailed expressions for the coordinate transformation as follows:

$$\begin{aligned} \begin{bmatrix} \Delta v_{Cd}{}^{ctrl} \\ \Delta v_{Cq}{}^{ctrl} \end{bmatrix} = \begin{bmatrix} \Delta v_{Cd} \\ \Delta v_{Cq} \end{bmatrix} &+ \begin{bmatrix} -\frac{3}{2}G_P v_{Cq0} i_{gd0} & -\frac{3}{2}G_P v_{Cq0} i_{gq0} \\ \frac{3}{2}G_P v_{Cd0} i_{gd0} & \frac{3}{2}G_P v_{Cd0} i_{gq0} \end{bmatrix} \begin{bmatrix} \Delta v_{Cd} \\ \Delta v_{Cq} \end{bmatrix} \\ &+ \begin{bmatrix} -\frac{3}{2}G_P v_{Cq0} v_{Cd0} & -\frac{3}{2}G_P v_{Cq0}{}^2 \\ \frac{3}{2}G_P v_{Cq0}{}^2 & \frac{3}{2}G_P v_{Cd0} v_{Cq0} \end{bmatrix} \begin{bmatrix} \Delta i_{gd} \\ \Delta i_{gq} \end{bmatrix} \end{aligned} \tag{17}$$

$$\begin{aligned} \begin{bmatrix} \Delta i_{Ld}{}^{ctrl} \\ \Delta i_{Lq}{}^{ctrl} \end{bmatrix} = \begin{bmatrix} \Delta i_{Ld} \\ \Delta i_{Lq} \end{bmatrix} &+ \begin{bmatrix} -\frac{3}{2}G_P i_{Lq0} i_{gd0} & -\frac{3}{2}G_P i_{Lq0} i_{gq0} \\ \frac{3}{2}G_P i_{Ld0} i_{gd0} & \frac{3}{2}G_P i_{Ld0} i_{gq0} \end{bmatrix} \begin{bmatrix} \Delta v_{Cd} \\ \Delta v_{Cq} \end{bmatrix} \\ &+ \begin{bmatrix} -\frac{3}{2}G_P i_{Lq0} v_{Cd0} & -\frac{3}{2}G_P i_{Lq0} v_{Cq0} \\ \frac{3}{2}G_P i_{Ld0} v_{Cd0} & \frac{3}{2}G_P i_{Ld0} v_{Cq0} \end{bmatrix} \begin{bmatrix} \Delta i_{gd} \\ \Delta i_{gq} \end{bmatrix} \end{aligned} \tag{18}$$

$$\begin{aligned} \begin{bmatrix} \Delta v_{cd} \\ \Delta v_{cq} \end{bmatrix} = \begin{bmatrix} \Delta v_{Cd}{}^{ctrl} \\ \Delta v_{Cq}{}^{ctrl} \end{bmatrix} &- \begin{bmatrix} -\frac{3}{2}G_P v_{cq0} i_{gd0} & -\frac{3}{2}G_P v_{cq0} i_{gq0} \\ \frac{3}{2}G_P v_{cd0} i_{gd0} & \frac{3}{2}G_P v_{cd0} i_{gq0} \end{bmatrix} \begin{bmatrix} \Delta v_{Cd} \\ \Delta v_{Cq} \end{bmatrix} \\ &- \begin{bmatrix} -\frac{3}{2}G_P v_{cq0} v_{Cd0} & -\frac{3}{2}G_P v_{cq0} v_{Cq0} \\ \frac{3}{2}G_P v_{cd0} v_{Cd0} & \frac{3}{2}G_P v_{cd0} v_{Cq0} \end{bmatrix} \begin{bmatrix} \Delta i_{gd} \\ \Delta i_{gq} \end{bmatrix} \end{aligned} \tag{19}$$

Similarly, the second-order matrices in (17) to (19) can be expressed: $\mathbf{B}_{vC\text{-}i}$, $\mathbf{B}_{vC\text{-}v}$, $\mathbf{B}_{iL\text{-}i}$, $\mathbf{B}_{iL\text{-}v}$, $\mathbf{B}_{vc\text{-}i}$, and $\mathbf{B}_{vc\text{-}v}$.

Conclusively, the systematic small-signal impedance model of the GFM grid-connected system containing physical circuits and control structures can be obtained by the above derivation process, as shown in Figure 2.

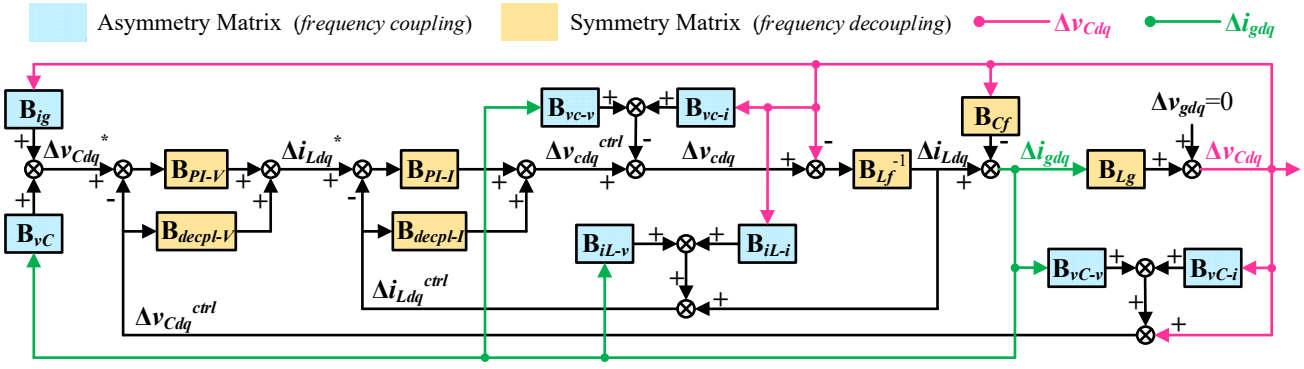


Figure 2. Small-signal impedance model of the GFM grid-connected system.

From Equations (1)–(3), as well as (12) and (13), it can be seen that the second-order matrices introduced by the physical circuit components of the system and the voltage and current inner control loops in the d-q frame coordinate system are symmetric matrices with no frequency coupling. These matrices can therefore also be referred to as frequency decoupling matrices, marked in yellow in the figure. On the other hand, as indicated by Equations (11) and (17)–(19), the frequency coupling terms in the system are primarily

introduced by the outer power control loops. The active power loop generates the power angle θ, which introduces frequency coupling through the Park transformation and Park inverse transformation. Meanwhile, the reactive power loop introduces frequency coupling due to the asymmetry in the *d*-*q* axis control. The frequency coupling introduced by the outer power loops is marked in blue in the figure.

According to Figure 2, the impedance of the GFM converter system $\boldsymbol{Z}_c(s)$ can be deduced as follows:

$$\begin{aligned} \boldsymbol{Z}_c(s) &= \frac{\Delta v_{Cdq}}{-\Delta i_{gdq}} \\ &= \frac{\boldsymbol{Z}_{c3}(s)+\mathbf{B}_{\boldsymbol{vc\text{-}v}}+\boldsymbol{Z}_{c2}(s)\mathbf{B}_{\boldsymbol{iL\text{-}v}}+\boldsymbol{Z}_{c1}(s)\mathbf{B}_{\boldsymbol{vC\text{-}v}}-\mathbf{B}_{\boldsymbol{PI\text{-}I}}\mathbf{B}_{\boldsymbol{PI\text{-}V}}\mathbf{B}_{\boldsymbol{vC}}}{\boldsymbol{I}+\boldsymbol{Z}_{c1}(s)+\boldsymbol{Z}_{c3}(s)\mathbf{B}_{\boldsymbol{Cf}}+\mathbf{B}_{\boldsymbol{vc\text{-}i}}+\boldsymbol{Z}_{c2}(s)\mathbf{B}_{\boldsymbol{iL\text{-}i}}+\boldsymbol{Z}_{c1}(s)\mathbf{B}_{\boldsymbol{vC\text{-}i}}-\mathbf{B}_{\boldsymbol{PI\text{-}I}}\mathbf{B}_{\boldsymbol{PI\text{-}V}}\mathbf{B}_{\boldsymbol{ig}}} \end{aligned} \tag{20}$$

where the expressions for $\boldsymbol{Z}_{c1}(s)$ to $\boldsymbol{Z}_{c3}(s)$ are the following:

$$\boldsymbol{Z}_{c1}(s) = \mathbf{B}_{\boldsymbol{PI\text{-}I}}\left(\mathbf{B}_{\boldsymbol{PI\text{-}V}} - \mathbf{B}_{\boldsymbol{decpl\text{-}V}}\right), \boldsymbol{Z}_{c2}(s) = \mathbf{B}_{\boldsymbol{PI\text{-}I}} - \mathbf{B}_{\boldsymbol{decpl\text{-}I}}, \boldsymbol{Z}_{c3}(s) = \mathbf{B}_{\boldsymbol{Lf}} + \mathbf{B}_{\boldsymbol{PI\text{-}I}} - \mathbf{B}_{\boldsymbol{decpl\text{-}I}} \tag{21}$$

For the sake of brevity, "(*s*)" will be omitted next. Expressing (20) in the form of a matrix:

$$\boldsymbol{Z}_{cdq} = \boldsymbol{Z}_c = \begin{bmatrix} Z_{cdq11} & Z_{cdq12} \\ Z_{cdq21} & Z_{cdq22} \end{bmatrix} \tag{22}$$

where $\boldsymbol{Z}_{cdq}$ represents the impedance matrix of the GFM converter system in the synchronous *d*-*q* frame, which contains four elements. Z_{cdq11} and Z_{cdq22} denote the self-impedance of the GFM converter in the *d*-*q* frame, while Z_{cdq12} and Z_{cdq21} denote the coupling impedance of the GFM converter in the *d*-*q* frame.

Transforming the *d*-*q* frame impedance matrix to the stationary frame provides clearer physical insights. According to the impedance transformation methods introduced in [22], the impedance matrix in the stationary frame can be expressed as follows:

$$\boldsymbol{Z}_{c\alpha\beta} = \frac{1}{2}\begin{bmatrix} 1 & j \\ 1 & -j \end{bmatrix} \boldsymbol{Z}_{cdq}(s - j\omega_1) \begin{bmatrix} 1 & 1 \\ -j & j \end{bmatrix} = \begin{bmatrix} Z_{c11} & Z_{c12} \\ Z_{c21} & Z_{c22} \end{bmatrix} \tag{23}$$

where $\omega_1 = 100\pi$ rad/s is the synchronous angular frequency, (s-$j\omega_1$) corresponds to the frequency shift required to transform from the synchronous *d*-*q* frame to a stationary frame. Z_{c11} and Z_{c22} denote the self-impedance of the GFM converter in the α-β stationary frame, while Z_{c12} and Z_{c21} denote the coupling impedance of the GFM converter in the α-β stationary frame.

Furthermore, the grid impedance matrix in the stationary frame is expressed as follows:

$$\boldsymbol{Z}_{g\alpha\beta} = \begin{bmatrix} R_g + sL_g & 0 \\ 0 & R_g + (s - j2\omega_1)L_g \end{bmatrix} = \begin{bmatrix} Z_{g11} & 0 \\ 0 & Z_{g22} \end{bmatrix} \tag{24}$$

where Z_{g11} and Z_{g22} denote the self-impedance of the grid in the α-β stationary frame, and there is no coupling impedance in the grid in the stationary coordinate system.

2.2. Impedance Frequency Scan Verification

To verify the correctness and accuracy of the obtained impedance model, the frequency scan based on a 200 kW GFM grid-connected system is carried out and compared with the tested data from the simulation model established in MATLAB/Simulink. The parameters of the applied GFM converter are shown in Table 1. By sequentially injecting positive and negative sequence disturbance voltage signals with frequencies ranging from 1 to 5 kHz, the positive-sequence impedance Z_{11}, negative-sequence impedance Z_{22}, and coupling impedance Z_{12} and Z_{21} at each frequency can be calculated by measuring the response of the current signals at the corresponding frequencies.

Table 1. Parameters of the applied GFM converter.

Parameter	Value	Parameter	Value
Rated voltage V_N	563 V	Droop gain m_p	0.02 p.u.
Rated power P_{ref}	200 kW	Droop gain n_q	0.08 p.u.
DC-side voltage V_{dc}	1300 V	Cut-off frequency ω_p	12.5 rad/s
Filter inductance L_f	300 µH	Cut-off frequency ω_q	50 rad/s
Filter resistance R_f	0.01 Ω	Voltage controller k_{p_V}	0.04 S
Filter capacitance C_f	35 µF	Voltage controller k_{i_V}	347 S/s
Short-circuit ratio *SCR*	1~7	Current controller k_{p_I}	1.26 Ω
R/X ratio of grid impedance R_g/X_g	0.1	Current controller k_{i_I}	420 Ω/s

The comparison between the theoretically derived values and the simulation results from the frequency scan measurement for the impedance model is illustrated in Figure 3. The impedance model obtained from theoretical derivation is plotted as a blue solid line, and the red asterisks are the simulation results. As can be seen from the figure, the simulation results closely match the mathematical model within the entire frequency range of interest, indicating that the impedance model derived mathematically in this paper is correct.

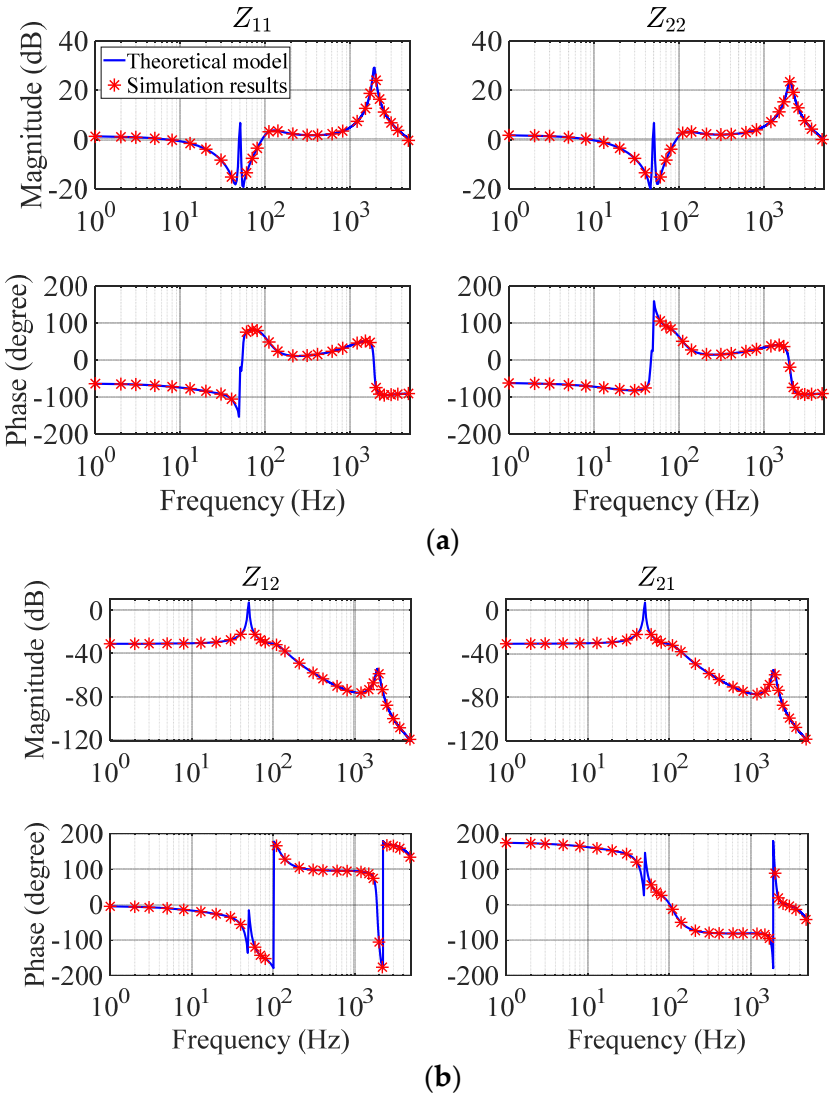


Figure 3. Validation of the impedance model by a frequency scan. (**a**) Diagonal elements (self-impedance); (**b**) off-diagonal elements (coupling impedance).

3. Analysis of Factors Affecting Coupling Impedance

From the impedance modeling of the GFM converter discussed in Section 2, it is evident that the outer power control loops play a key role in introducing frequency coupling. More specifically, this is reflected in three main aspects: the active power loop gain G_P, the reactive power loop gain G_Q, and the steady-state operating points. Therefore, this section will focus on these three areas, analyzing their respective impacts on the coupling impedances Z_{12} and Z_{21} of the GFM converter.

3.1. Effect of Steady-State Operating Point on Coupling Impedance

It is evident from Equations (11) and (17)–(19) that the values of the steady-state operating points affect the corresponding frequency coupling matrices. Therefore, this part focuses on the impedance characteristics of the coupling impedance under different active power levels P_{ref} to analyze the impact of various steady-state operating points on frequency coupling.

It can be seen from Figure 4 that the magnitude of the coupling impedance is larger at high power levels compared to low power levels. Therefore, the frequency coupling is stronger at high power levels. In addition, the phase curves of the coupling impedance in the low-frequency range vary considerably at different power levels. Therefore, the different steady-state operating points will have a large impact on the impedance characteristics of the coupling impedance.

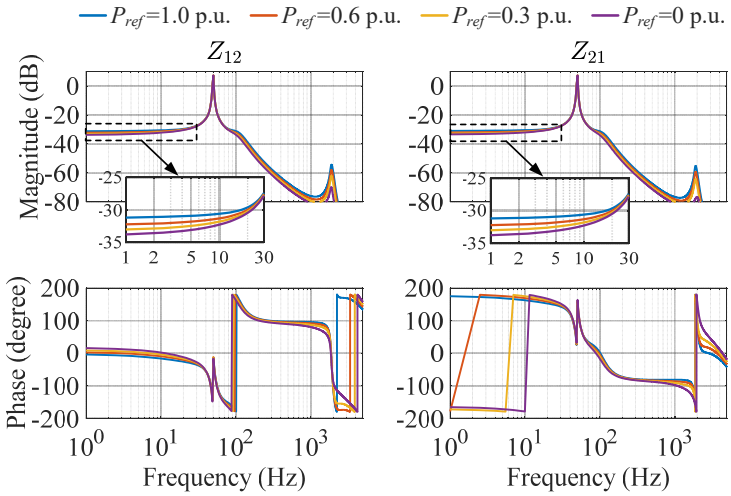


Figure 4. Impact of different power levels P_{ref} on coupling impedance with SCR = 7.

3.2. Effect of Active Power Loop on Coupling Impedance

From Equations (17)–(19), it can be observed that the frequency coupling introduced by the active power loop is primarily influenced by the loop gain G_P. More specifically, G_P is determined by the droop coefficient m_p and the cut-off frequency ω_p of the low-pass filter. Therefore, the following analysis will focus on analyzing the effect of the variation of m_p and ω_p parameters on the coupling impedance. The variation of m_p is required to remain within the standard range specified by grid codes [23]. It is worth noting that when one parameter changes, the other parameters remain consistent with Table 1.

Figure 5 illustrates the coupling impedance curves of the GFM converter as the active power loop parameters m_p and ω_p vary. From the figure, it can be observed that the magnitude–frequency curves of the coupling impedance under different active power loop parameters largely overlap, with only slight variations in the frequency range near the fundamental frequency. This indicates that changes in the active power loop parameters have minimal impact on the coupling impedance. Therefore, variations in either m_p or ω_p within the active power loop will not significantly affect frequency coupling.

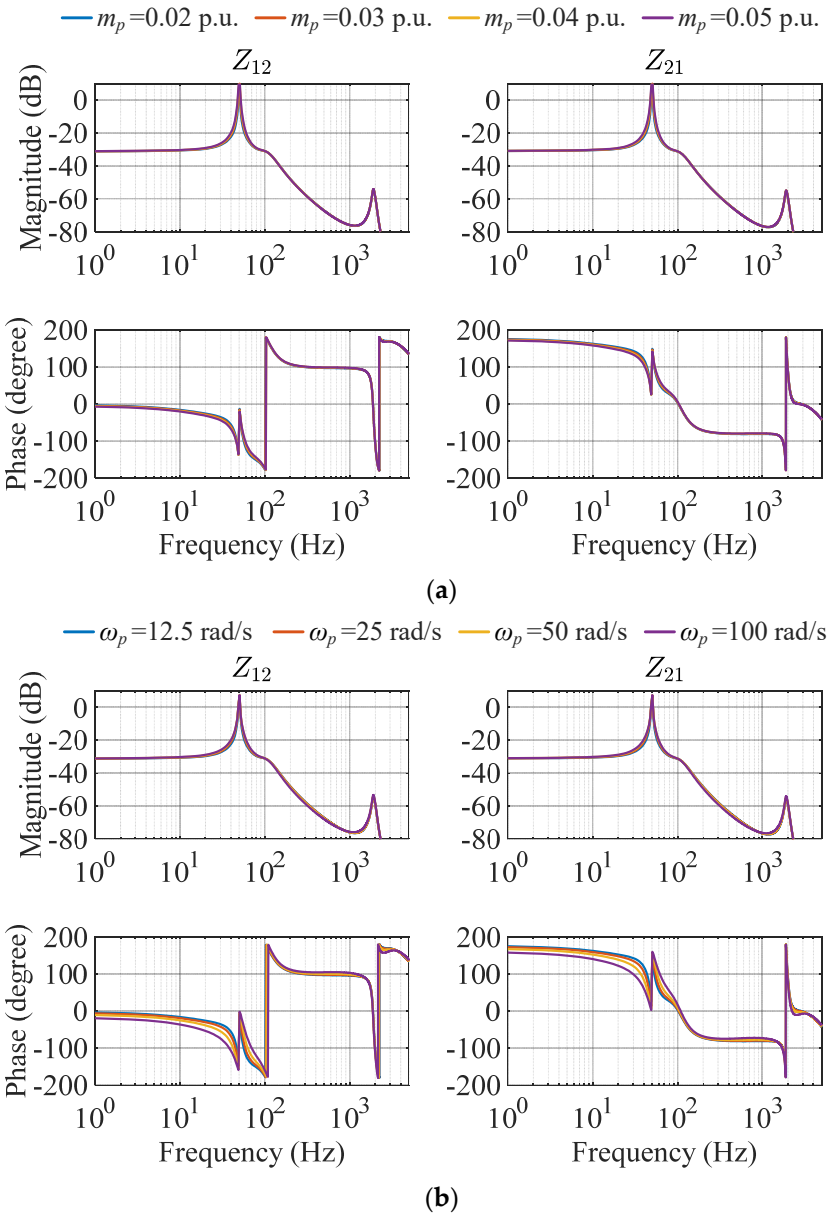


Figure 5. Impact of different active power loop parameters on coupling impedance at P_{ref} = 1.0 p.u. with SCR = 3. (**a**) Different m_p; (**b**) different ω_p.

3.3. Effect of Reactive Power Loop on Coupling Impedance

Similarly, the frequency coupling introduced by the reactive power loop is primarily influenced by the loop gain G_Q, which is determined by the droop coefficient n_q and the cut-off frequency ω_q of the low-pass filter. The following analysis will focus on analyzing the effect of the variation of n_q and ω_q parameters on the coupling impedance. The variation of n_q is required to remain within the standard range specified by grid codes [23].

Figure 6 illustrates the coupling impedance curves of the GFM converter as the reactive power loop parameters n_q and ω_q vary. From the figure, it can be seen that when the reactive power loop parameters n_q or ω_q increase, the magnitude of the coupling impedance curve shifts upwards, indicating a higher degree of frequency coupling in the system. The results suggest that the degree of frequency coupling is most sensitive to changes in the reactive power loop parameters, and reducing these parameters can effectively decrease the extent of frequency coupling in the system.

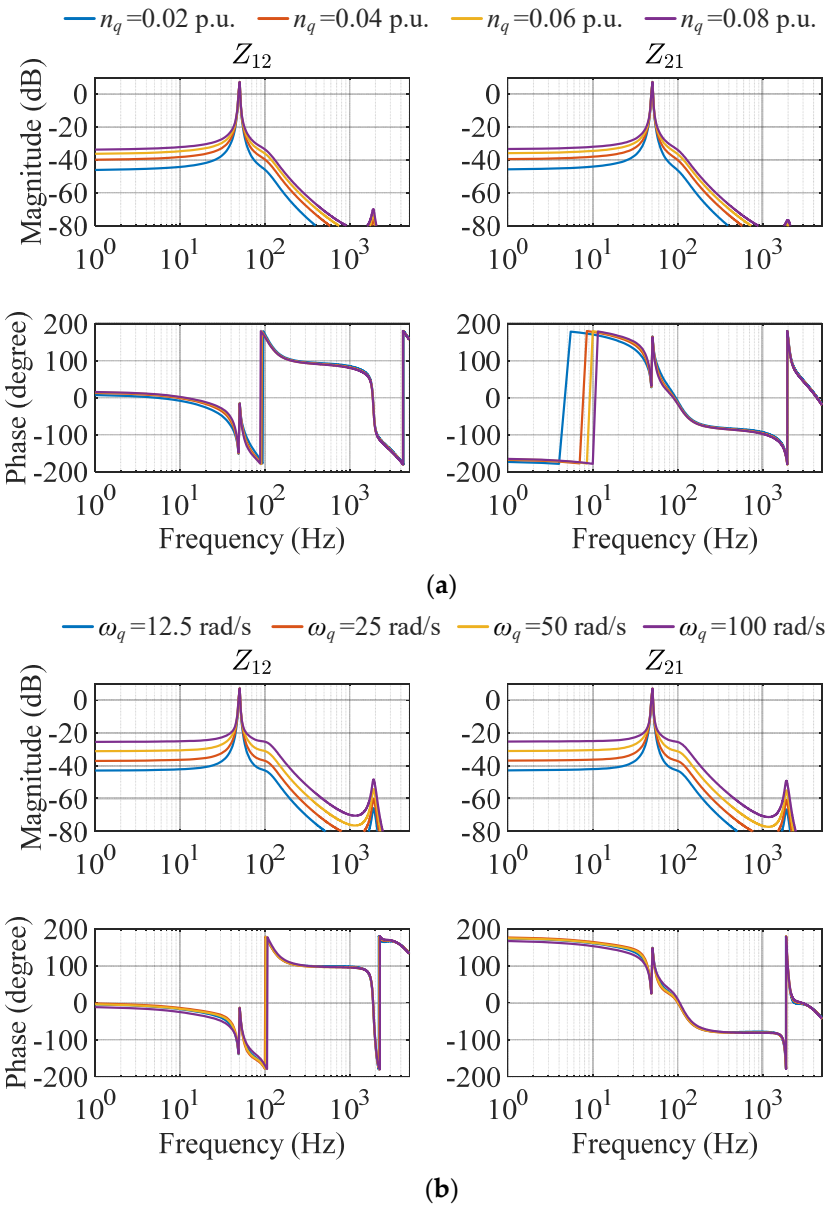


Figure 6. Impact of different reactive power loop parameters on coupling impedance at P_{ref} = 0.1 p.u. with SCR = 7. (**a**) Different n_q; (**b**) different ω_q.

In summary, both the power control loop gains and the steady-state operating points affect the coupling impedance of GFM converters, leading to the following conclusions:

(1) The reactive power loop gain G_Q is the most sensitive to frequency coupling, and the larger the parameters n_q and ω_q, the greater the degree of frequency coupling;
(2) The changes in the steady-state operating points also influence frequency coupling, with the degree of frequency coupling gradually increasing as the power level P_{ref} rises;
(3) The variations in the active power loop gain G_P have minimal impact on frequency coupling, with only slight effects observed near the fundamental frequency.

4. Stability Analysis and Simulation Validation

Section 3 analyzed the factors influencing frequency coupling and examined the impedance characteristics of the coupling impedance under various parameter conditions. Building on Section 3, the stability analysis and simulation verification are carried out

for the aspects affecting the frequency coupling under different parameter conditions in this section.

The effect of frequency coupling means that the GFM grid-connected system can no longer be represented by a simple single-input single-output (SISO) model but must instead be treated as a two-dimensional multiple-input multiple-output (MIMO) system. As a result, all transfer functions of the system are expressed as "2 × 2" matrices, requiring the use of the Generalized Nyquist Criterion (GNC) for stability analysis [24]. The impedance ratio of the grid-connected converter system is normally used for stability analysis by GNC. As the external characteristic exhibited by the GFM is a voltage source, the impedance ratio can be expressed as the impedance of the GFM divided by the grid impedance:

$$\boldsymbol{L} = \frac{\boldsymbol{Z}_{c\alpha\beta}}{\boldsymbol{Z}_{g\alpha\beta}} = \frac{\begin{bmatrix} Z_{c11} & Z_{c12} \\ Z_{c21} & Z_{c22} \end{bmatrix}}{\begin{bmatrix} Z_{g11} & 0 \\ 0 & Z_{g22} \end{bmatrix}} = \begin{bmatrix} \frac{Z_{c11}}{Z_{g11}} & \frac{Z_{c12}}{Z_{g22}} \\ \frac{Z_{c21}}{Z_{g11}} & \frac{Z_{c22}}{Z_{g22}} \end{bmatrix} = \begin{bmatrix} L_{11} & L_{12} \\ L_{21} & L_{22} \end{bmatrix} \tag{25}$$

Theorem 1. *Assuming* $\boldsymbol{L}$ *has no right-half-plane poles, the grid-connected converter system is asymptotically stable if and only if the characteristic loci (Nyquist curves) for the eigenvalues of* $\boldsymbol{L}$*, i.e.,*

$$\lambda_{1,2} = \frac{L_{11} + L_{22} \pm \sqrt{(L_{11} - L_{22})^2 + 4L_{12}L_{21}}}{2} \tag{26}$$

taken together, do not encircle (−1, j0) for $s = j\omega$, $-\infty < \omega < \infty$.

From Equation (26), it can be seen that the impact of frequency coupling is reflected in the coupling impedance, represented by the term $L_{12}L_{21}$. Therefore, if the frequency coupling is not considered, the stability of the system may even be misjudged in the GNC analysis.

4.1. Stability Analysis and Simulation Validation under Different Steady-State Operating Points

Based on the aforementioned theoretical analysis, the GFM system with and without frequency coupling is analyzed under stability using the GNC at different power levels, respectively, as shown in Figure 7. With the frequency coupling considered, the GNC curves do not encircle (−1, j0) at P_{ref} = 1.0 p.u., which indicates that the system is stable. Also, the GNC curves encircle (−1, j0) at P_{ref} = 0.1 p.u., indicating that the system is unstable, as illustrated in Figure 7a. However, in Figure 7b, the GNC curves are presented without considering the effect of frequency coupling, which is L_{12} and L_{21} = 0. It can be seen that the GNC curves encircle (−1, j0) at either P_{ref} = 1.0 p.u. or 0.1 p.u., indicating that the system is unstable at both power levels. Therefore, whether frequency coupling is considered or not can lead to different results in GNC stability analysis.

Given the differing stability analysis results of the GNC when considering or neglecting frequency coupling, the following simulation is carried out to verify the results at different power levels. Figure 8 shows the simulation results of the system at different power levels P_{ref}. Figure 8a shows the steady-state waveforms of PCC voltage, grid current, and active power at P_{ref} = 1.0 p.u., and Figure 8b shows the steady-state waveforms at P_{ref} = 0.1 p.u. The active power can accurately track the reference signal at P_{ref} = 1.0 p.u. and the system can maintain a stable state as shown in Figure 8a. It is seen that the currents are purely sinusoidal; neither harmonic components nor an imbalance phenomenon exist. In contrast, it can be seen that oscillation occurs at P_{ref} = 0.1 p.u. and causes instability of the system as shown in Figure 8b. In this case, the FFT analysis shows that in the current there is a sub-synchronous harmonic component of 36 Hz, and a harmonic component of 64 Hz is also present due to the frequency coupling effect. Consequently, the active power exhibits the phenomenon of sub-synchronous oscillation with an oscillation frequency of 14 Hz.

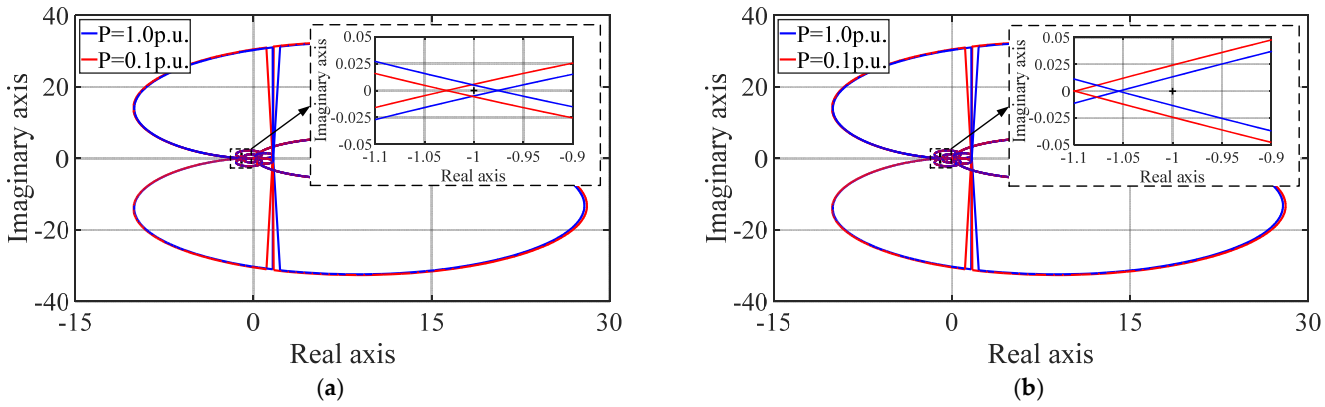


Figure 7. GNC diagrams of GFM at different power levels. (**a**) Considering frequency coupling; (**b**) without considering frequency coupling.

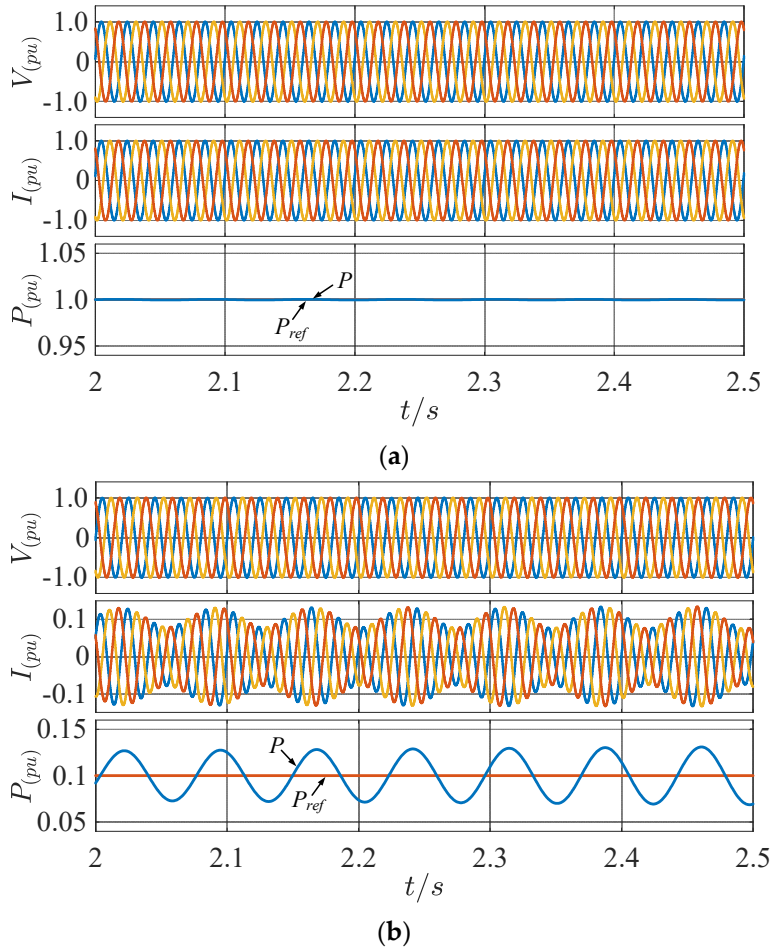


Figure 8. Simulation results of the system at different power levels with SCR = 7. (**a**) P_{ref} = 1.0 p.u.; (**b**) P_{ref} = 0.1 p.u.

The simulation results are consistent with the GNC stability analysis considering frequency coupling, as described in Figure 7a. Therefore, neglecting frequency coupling can lead to inaccuracies in GNC stability assessments, making it essential to consider this factor in the analysis. Consequently, in the subsequent GNC stability analysis, frequency coupling, specifically the effect of coupling impedance, will be considered.

4.2. Stability Analysis and Simulation Validation under Different Active Power Loop Parameters

Figures 9a and 10a present the GNC stability analysis for variations in the active power loop parameters, with the GFM converter operating at the rated operating point of SCR = 3. It is important to note that the figures only show the extreme values of the parameters m_p and ω_p within the standard range specified by grid codes. As observed, regardless of changes in m_p or ω_p, the GNC curves do not encircle $(-1, j0)$, indicating that the system remains stable throughout. Additionally, the GNC curves remain almost identical when m_p or ω_p changes, suggesting that variations in the active power loop parameters have minimal impact on the impedance model of the GFM converter. The observation aligns with the conclusion in Section 3.2 that the impedance characteristics of the GFM are largely unaffected by changes in the active power loop parameters.

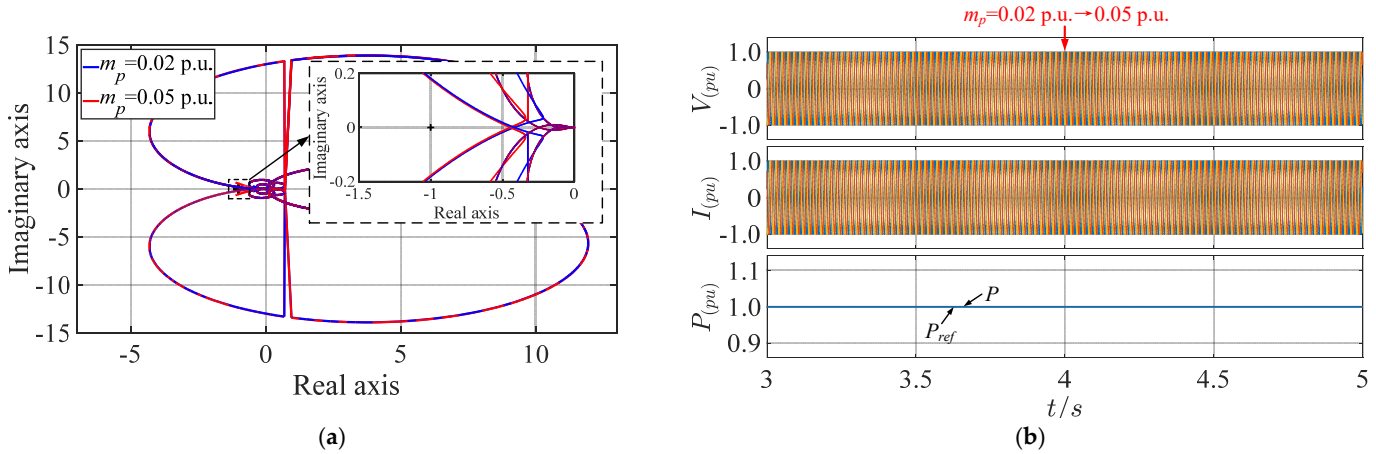


Figure 9. Simulation results and GNC stability analysis when m_p is varied at the P_{ref} = 1.0 p.u. operating condition with SCR = 3. (**a**) Simulation results; (**b**) GNC stability analysis.

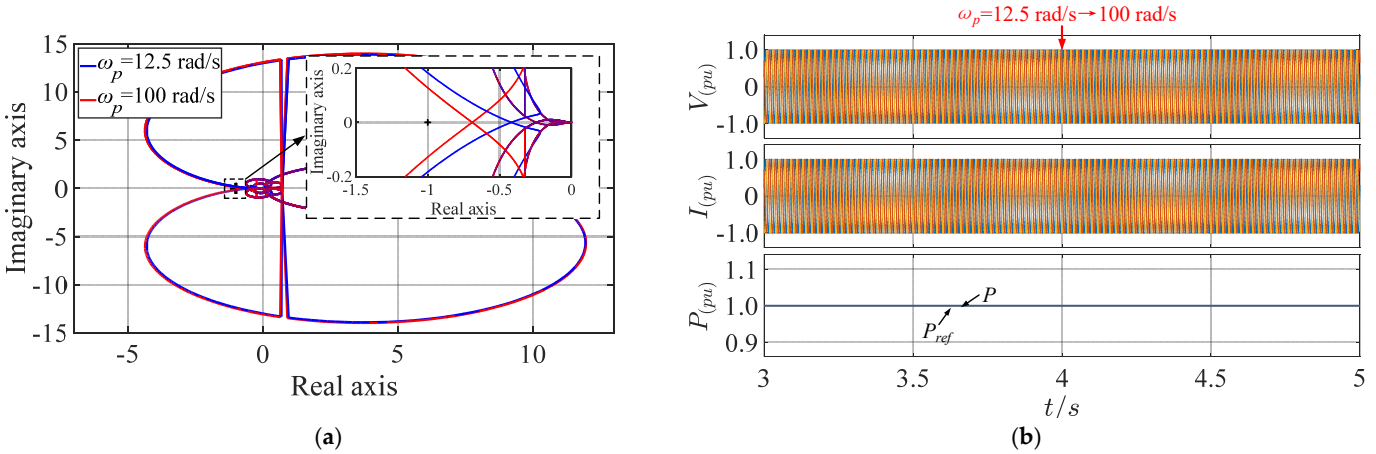


Figure 10. Simulation results and GNC stability analysis when ω_p is varied at the P_{ref} = 1.0 p.u. operating condition with SCR = 3. (**a**) Simulation results; (**b**) GNC stability analysis.

Figures 9b and 10b provide the corresponding simulation verification results. Taking Figure 9b as an example, the active power loop droop coefficient m_p is maintained at 0.02 p.u. before 4 s, and the system remains stable. At the moment of 4 s, m_p suddenly increases to 0.05 p.u., yet the system continues to operate stably, with no significant fluctuations in output voltage, current, or power. Similarly, when the active power loop parameter ω_p changes, the system can remain stable. The simulation results are consistent with the conclusions drawn from the GNC stability analysis.

4.3. Stability Analysis and Simulation Validation under Different Reactive Power Loop Parameters

Similarly, Figures 11a and 12a present the GNC stability analysis for variations in the reactive power loop parameters, with the GFM converter operating at a low operating point of P_{ref} = 0.1 p.u. with SCR = 7. As seen in the figures, when the values of n_q and ω_q are large, the GNC curve encloses (−1, j0), indicating that the system is in an unstable state. Conversely, when n_q and ω_q are smaller, the GNC curve does not enclose (−1, j0), indicating that the system remains stable. Additionally, there are significant differences in the GNC curves as n_q or ω_q change, suggesting that variations in the reactive power loop parameters have a substantial impact on the impedance model of the GFM converter. The observation aligns with the conclusion in Section 3.3 that the impedance characteristics of the GFM are significantly affected by changes in reactive power loop parameters.

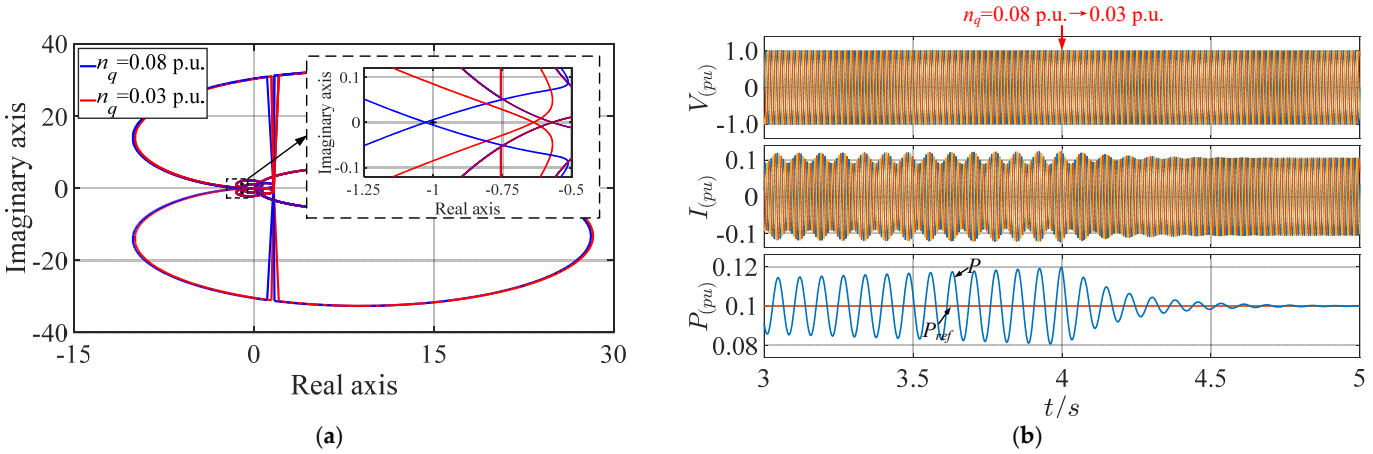


Figure 11. Simulation results and GNC stability analysis when n_q is varied at the P_{ref} = 0.1 p.u. operating condition with SCR = 7. (**a**) Simulation results; (**b**) GNC stability analysis.

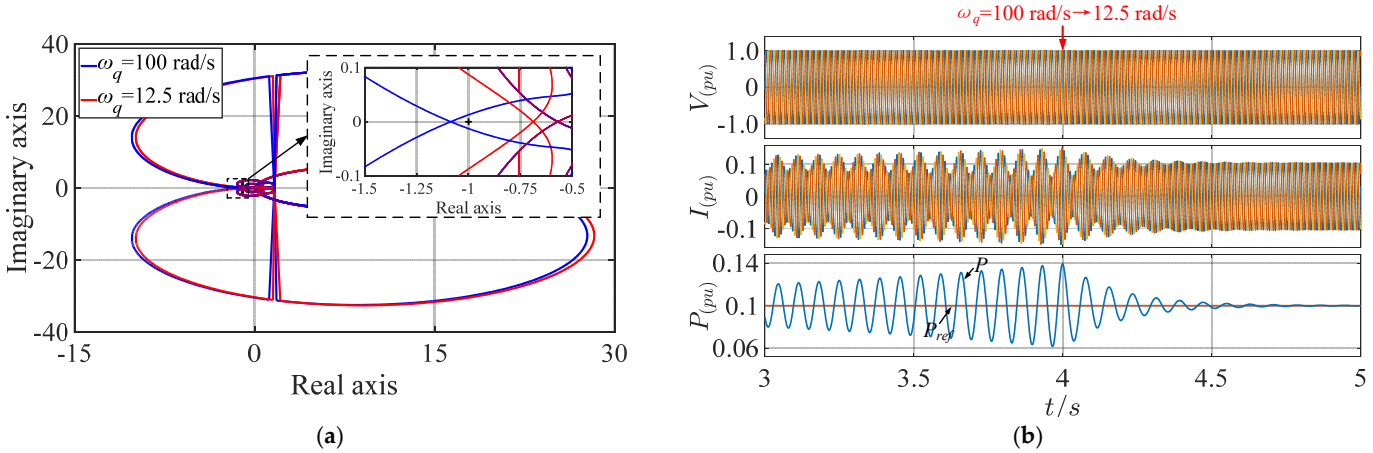


Figure 12. Simulation results and GNC stability analysis when ω_q is varied at the P_{ref} = 0.1 p.u. operating condition with SCR = 7. (**a**) Simulation results; (**b**) GNC stability analysis.

Figures 11b and 12b provide the corresponding simulation verification results. Taking Figure 11b as an example, the reactive power loop droop coefficient n_q is maintained at 0.08 p.u. before 4 s, and it is evident that the output power exhibits sub-synchronous oscillations, indicating that the system is in an unstable state. At the moment of 4 s, n_q suddenly reduces to 0.03 p.u., and the system gradually returns to a stable state. The simulation results are consistent with the conclusions drawn from the GNC stability analysis.

5. Conclusions

This paper focuses on the GFM converters under various grid conditions, deriving and validating a systematic impedance model that accounts for frequency coupling characteristics. The analysis identifies the outer power control loop and steady-state operating points as the primary causes of frequency coupling in GFM converters. Specifically, the steady-state operating points predominantly affect the coupling behavior, apart from the fundamental frequency. The active power loop influences characteristics near the fundamental frequency, while the reactive power loop impacts the entire frequency spectrum. Notably, the low operating points instead lead to a destabilizing phenomenon of system oscillations, which can be damped by adjusting the parameters of the reactive power loop. Furthermore, the Generalized Nyquist Criterion analysis shows the necessity of considering frequency coupling in stability assessments of GFM converters to avoid inaccurate stability conclusions. Finally, time–domain simulations validate the conclusions drawn from the Generalized Nyquist Criterion stability analysis.

Future work will focus on exploring the applicability of frequency coupling in stability criteria. This research aims to establish a new criterion that defines the conditions under which the influence of coupling impedance must be considered and when it can be disregarded. Such a criterion will enable more straightforward and efficient stability assessments, allowing for a clearer understanding of when coupling impedance is essential for system stability evaluation and when it can be safely ignored.

Author Contributions: Methodology, H.T.; software, J.W.; validation, C.W.; writing—original draft, H.T.; supervision, Y.W. All authors have read and agreed to the published version of the manuscript.

Funding: This research received no external funding.

Data Availability Statement: The original contributions presented in the study are included in the article, further inquiries can be directed to the corresponding author.

Conflicts of Interest: The authors declare no conflicts of interest.

References

1. Bahrani, B.; Ravanji, M.H.; Kroposki, B.; Ramasubramanian, D.; Guillaud, X.; Prevost, T.; Cutululis, N.-A. Grid-Forming Inverter-Based Resource Research Landscape: Understanding the Key Assets for Renewable-Rich Power Systems. *IEEE Power Energy Mag.* **2024**, *22*, 18–29. [CrossRef]
2. Pan, D.; Wang, X.; Liu, F.; Shi, R. Transient Stability of Voltage-Source Converters With Grid-Forming Control: A Design-Oriented Study. *IEEE J. Emerg. Sel. Top. Power Electron.* **2020**, *8*, 1019–1033. [CrossRef]
3. Rosso, R.; Wang, X.; Liserre, M.; Lu, X.; Engelken, S. Grid-Forming Converters: Grid-Synchronization, and Future Trends—A Review. *IEEE Open J. Ind. Appl.* **2021**, *2*, 93–109. [CrossRef]
4. Xin, H.; Huang, L.; Zhang, L.; Wang, Z.; Hu, J. Synchronous instability mechanism of p-f droop-controlled voltage source converter caused by current saturation. *IEEE Trans. Power Syst.* **2016**, *31*, 5206–5207. [CrossRef]
5. Chen, J.; O'Donnell, T. Parameter Constraints for Virtual Synchronous Generator Considering Stability. *IEEE Trans. Power Syst.* **2019**, *34*, 2479–2481. [CrossRef]
6. Huang, L.; Xin, H.; Wang, Z.; Wu, K.; Wang, H.; Hu, J.; Lu, C. A Virtual Synchronous Control for Voltage-Source Converters Utilizing Dynamics of DC-Link Capacitor to Realize Self-Synchronization. *IEEE J. Emerg. Sel. Top. Power Electron.* **2017**, *5*, 1565–1577. [CrossRef]
7. Johnson, B.B.; Dhople, S.V.; Hamadeh, A.O.; Krein, P.T. Synchronization of parallel single-phase inverters with virtual oscillator control. *IEEE Trans. Power Electron.* **2014**, *29*, 6124–6138. [CrossRef]
8. Li, Y.; Vilathgamuwa, D.; Loh, P.C. Design, analysis, and real-time testing of a controller for multibus microgrid system. *IEEE Trans. Power Electron.* **2004**, *19*, 1195–1204. [CrossRef]
9. Fan, B.; Liu, T.; Zhao, F.; Wu, H.; Wang, X. Review of Current-Limiting Control of Grid-Forming Inverters Under Symmetrical Disturbances. *IEEE Open J. Power Electron.* **2022**, *3*, 955–969. [CrossRef]
10. Liao, Y.; Wang, X.; Blaabjerg, F. Passivity-Based Analysis and Design of Linear Voltage Controllers For Voltage-Source Converters. *IEEE Open J. Ind. Electron. Soc.* **2020**, *1*, 114–126. [CrossRef]
11. Li, C.; Yang, Y.; Cao, Y.; Wang, L.; Dragicevic, T.; Blaabjerg, F. Frequency and Voltage Stability Analysis of Grid-Forming Virtual Synchronous Generator Attached to Weak Grid. *IEEE J. Emerg. Sel. Top. Power Electron.* **2022**, *10*, 2662–2671. [CrossRef]
12. Wu, H.; Ruan, X.; Yang, D.; Chen, X.; Zhao, W.; Lv, Z.; Zhong, Q.-C. Small-Signal Modeling and Parameters Design for Virtual Synchronous Generators. *IEEE Trans. Ind. Electron.* **2016**, *63*, 4292–4303. [CrossRef]

13. Liao, Y.; Wang, X.; Liu, F.; Xin, K.; Liu, Y. Sub-Synchronous Control Interaction in Grid-Forming VSCs with Droop Control. In Proceedings of the 2019 4th IEEE Workshop on the Electronic Grid (eGRID), Xiamen, China, 11–14 November 2019; pp. 1–6.
14. Rodriguez, P.; Candela, I.; Citro, C.; Rocabert, J.; Luna, A. Control of grid-connected power converters based on a virtual admittance control loop. In Proceedings of the 2013 15th European Conference on Power Electronics and Applications (EPE), Lille, France, 3–5 September 2013; pp. 1–10.
15. Zhao, F.; Wang, X.; Zhu, T. Low-Frequency Passivity-Based Analysis and Damping of Power-Synchronization Controlled Grid-Forming Inverter. *IEEE J. Emerg. Sel. Top. Power Electron.* **2023**, *11*, 1542–1554. [CrossRef]
16. Wu, W.; Chen, Y.; Zhou, L.; Luo, A.; Zhou, X.; He, Z.; Yang, L.; Xie, Z.; Liu, J.; Zhang, M.; et al. Sequence Impedance Modeling and Stability Comparative Analysis of Voltage-Controlled VSGs and Current-Controlled VSGs. *IEEE Trans. Ind. Electron.* **2019**, *66*, 6460–6472. [CrossRef]
17. Wu, W.; Zhou, L.; Chen, Y.; Luo, A.; Dong, Y.; Zhou, X.; Xu, Q.; Yang, L.; Guerrero, J.M. Sequence-Impedance-Based Stability Comparison Between VSGs and Traditional Grid-Connected Inverters. *IEEE Trans. Power Electron.* **2019**, *34*, 46–52. [CrossRef]
18. Peng, Y.; Yin, T.; Li, M.; Wang, Y.; Hu, D.; Liu, Z. A Sequence Impedance Modeling of VSG With Consideration of Inner Loops Control. In Proceedings of the 2019 4th IEEE Workshop on the Electronic Grid (eGRID), Xiamen, China, 11–14 November 2019; pp. 1–5.
19. Shi, K.; Wang, Y.; Sun, Y.; Xu, P.; Gao, F. Frequency-Coupled Impedance Modeling of Virtual Synchronous Generators. *IEEE Trans. Power Syst.* **2021**, *36*, 3692–3700. [CrossRef]
20. Chen, J.; Zhang, X.; Yang, Y.; Chen, J.; Chen, X. Impedance modelling and grid integration stability evaluation of three-phase virtual synchronous generator. *IET Power Electron.* **2022**, *15*, 80–91. [CrossRef]
21. Pedra, J.; Sainz, L.; Monjo, L. Review and Improvements to the Measurements of the VSC Impedance Transfer Matrix. *IEEE Trans. Power Deliv.* **2024**, *39*, 1283–1298. [CrossRef]
22. Wang, X.; Harnefors, L.; Blaabjerg, F. Unified Impedance Model of Grid-Connected Voltage-Source Converters. *IEEE Trans. Power Electron.* **2018**, *33*, 1775–1787. [CrossRef]
23. White Paper: Grid Forming Functional Specifications for BPS-Connected Battery Energy Storage Systems. NERC, September 2023. [Online]. Available online: https://www.nerc.com/ (accessed on 1 September 2023).
24. Harnefors, L. Modeling of Three-Phase Dynamic Systems Using Complex Transfer Functions and Transfer Matrices. *IEEE Trans. Ind. Electron.* **2007**, *54*, 2239–2248. [CrossRef]

Disclaimer/Publisher's Note: The statements, opinions and data contained in all publications are solely those of the individual author(s) and contributor(s) and not of MDPI and/or the editor(s). MDPI and/or the editor(s) disclaim responsibility for any injury to people or property resulting from any ideas, methods, instructions or products referred to in the content.